Nanoscale

ROYAL SOCIETY OF CHEMISTRY

PAPER

View Article Online
View Journal | View Issue

Cite this: *Nanoscale*, 2024, **16**, 7419

Bright near-infrared emission from the $Au_{39}(SR)_{29}$ nanocluster†

Zhongyu Liu, ‡[a] Lianshun Luo, ‡[a] Jie Kong, [b] Ellen Kahng,[a] Meng Zhou [b] and Rongchao Jin *[a]

Received 17th February 2024,
Accepted 15th March 2024

DOI: 10.1039/d4nr00677a

rsc.li/nanoscale

The synthesis of atomically precise gold nanoclusters with high photoluminescence quantum yield (PLQY) in the near-infrared (NIR) region and understanding their photoluminescence mechanism are crucial for both fundamental science and practical applications. Herein, we report a highly luminescent, molecularly pure $Au_{39}(PET)_{29}$ (PET = 2-phenylethanethiolate) nanocluster with PLQY of 19% in the NIR range (915 nm). Steady state and time-resolved PL analyses, as well as temperature-dependent PL measurements reveal the emission nature of $Au_{39}(PET)_{29}$, which consists of prompt fluorescence (weak), thermally activated delayed fluorescence (TADF), and phosphorescence (predominant). Furthermore, strong dipole–dipole interaction in the solid-state (*e.g.*, $Au_{39}(PET)_{29}$ nanoclusters embedded in a polystyrene thin-film) is found to narrow the energy gap between the S_1 and T_1 states, which results in faster intersystem crossing and reverse intersystem crossing; thus, the ratio of TADF to phosphorescence varies and the total PLQY is increased to 32%. This highly luminescent nanocluster holds promise in imaging, sensing and optoelectronic applications.

Introduction

Atomically precise metal nanoclusters (NCs) have attracted much attention owing to their intriguing electronic structure and rich properties.[1–6] In recent studies on the electronic and optical properties of NCs, photoluminescence has become one of the thrusts.[3,4,6–25] Unlike organic dyes and quantum dots, the emission of gold nanoclusters exhibits a larger Stokes shift and falls in the near-infrared (NIR, 800–2500 nm).[8,20,22,24–30] The NIR luminescence, high stability and good biocompatibility of gold nanoclusters make them ideal candidates for applications in bioimaging,[22,23] medicine,[31,32] and optoelectronics.[6]

With the successful development of synthetic methods such as size focusing and transformation,[33–35] molecularly pure, thiolate-protected gold NCs have been achieved.[1] However, the photoluminescence quantum yields (PLQY) of most gold NCs are quite low. For instance, the PLQY of the icosahedral $Au_{25}(SR)_{18}^-$, bi-icosahedral $Au_{38}(SR)_{24}$, face-centered-cubic $Au_{28}(SR)_{20}$, $Au_{36}(SR)_{24}$, $Au_{44}(SR)_{28}$ and cuboctahedral $Au_{23}(SR)_{16}^-$ are all found to be only ~1%.[27,30,36–39] While the $Au_{22}(SG)_{18}$ and $Au_{10}(SR)_6$ show very high PLQY after surface engineering,[3,4] their emissions are in the visible range. In the NIR region, only few thiolate-protected gold nanoclusters with atomic precision have been found to have PLQY higher than 10%, including the body-centered-cubic Au_{38} NC with a 15% PLQY in the NIR reported by Li *et al.*,[26] and the rod-shaped Au_{42} NC with a 12% PLQY of dual emission in the NIR reported by Luo *et al.*[40] Therefore, strong emission is still highly desirable for thiolate-protected gold NCs and worth significant efforts.

Several strategies have been developed to improve the PLQY of gold NCs. Xie's group reported an aggregation-induced emission mechanism and found that it can significantly increase the PLQY of a series of gold NCs.[41,42] This aggregation-induced enhancement was also studied by the groups of Nieh, Zang and Zhu.[22,43–45] A related crystallization-induced emission enhancement was found in Au_8 NCs by the Sun group.[46] Lee and coworkers reported a surface rigidifying strategy for achieving highly luminescent Au_{22} NCs.[3] Tsukuda's group found that heteroatom doping in $Au_{25}(SR)_{18}$ can tune the electron distribution and increase the stiffness of the Au_{13} inner core and hence largely improve the PLQY.[39] They also found that the mechanism can be applied to phosphine-protected Au_{13} NCs.[47,48] Moreover, ligand engineering was introduced by Jin's group[49] to improve the PLQY of $Au_{25}(SR)_{18}$ and has been proved to be a facile and universal strategy in recent work.[50–53]

[a]*Department of Chemistry, Carnegie Mellon University. Pittsburgh, PA 15213, USA. E-mail: rongchao@andrew.cmu.edu*
[b]*Hefei National Laboratory for Physical Sciences at the Microscale, Department of Chemical Physics, University of Science and Technology of China. Hefei, Anhui 230026, China*

†Electronic supplementary information (ESI) available: Details of the synthesis and spectroscopic characterization, supporting Fig. S1–11. See DOI: https://doi.org/10.1039/d4nr00677a

‡These authors contributed equally to this work.

Understanding the PL mechanism of gold NCs is crucial for improving their PLQY. However, the excited state electron dynamics of gold NCs is much more complicated than conventional luminescent materials and requires careful analysis.[30,54] In recent work, Li *et al.* reported a photo-induced structural distortion accompanied by electron redistribution in three bi-tetrahedral gold NCs.[55] Fluorescence and phosphorescence may coexist in the NCs[40] and their conversion has also been reported by Konishi.[15] Wang's group identified a thermally activated delayed fluorescence (TADF) in alkynyl-protected Au_{22} NCs,[10] and TADF also exists in Ag_{22} NCs.[12] Therefore, the PL mechanism of gold NCs is quite complicated, and both the core structure[6,7] and the ligands[28,50] of NCs are involved in the PL processes.

Herein, we report an $Au_{39}(PET)_{29}$ NC with strong emission in the NIR and PLQY of 19% in solution and 32% in films at room temperature. Combining the room temperature time-resolved PL measurements and temperature-dependent PL analysis, we reveal that the room temperature PL of $Au_{39}(PET)_{29}$ consists of three components: nanosecond prompt fluorescence (weak), sub-microsecond TADF, and microsecond phosphorescence (predominant). Further analysis identifies an ultrasmall gap between the singlet and triplet states (~50 meV), hence, an overlap of fluorescence and phosphorescence peaks in the PL spectrum. By embedding $Au_{39}(PET)_{29}$ NCs in polystyrene (PS) thin-films, much faster intersystem crossing and reverse intersystem crossing are resulted. Overall, the attainment of a highly NIR-luminescent nanocluster and mechanistic insights promotes the fundamental understanding of the PL of NCs and the development of their future applications.

Results and discussion

Synthesis and mass spectrometry characterization

The $Au_{39}(PET)_{29}$ NC was synthesized by a facile one-pot protocol that involves two primary steps: (1) the reaction between a NHC–Au–Br complex (NHC = N-heterocyclic carbene) and phenylethanethiol, which yields white insoluble Au(I)-SR complexes, and (2) a slow reduction of Au(I)-SR complexes using excess $(CH_3)_3CNH_2{\cdot}BH_3$. The utilization of NHC–Au–Br complexes for kinetic control of Au(I)-SR polymer generation, alongside the weak reducing properties of $(CH_3)_3CNH_2BH_3$ compared to $NaBH_4$, facilitated the successful synthesis of the Au_{39} nanocluster. Additionally, the ease of modifying the nitrogen substituents adjacent to the carbenic carbon in NHC allows for precise manipulation of electron density, thereby enabling accurate regulation of mass distribution in the generated Au(I)-SR polymers, a process being difficult to achieve with traditional thiol-Au and phosphine-Au complexes. After removing the solvent and washing with methanol, a black crude product was obtained (see ESI† for details). Pure $Au_{39}(PET)_{29}$ was isolated from the crude product by thin-layer chromatography (TLC) (Fig. S1†). Electrospray ionization (ESI) mass spectrometry was performed to determine the formula of the as-obtained gold NC. Four characteristic peaks at *m/z* 5830.70, 5963.63, 11 661.20 and 11 793.89 are observed (Fig. 1A), which are identified as $[Au_{39}(PET)_{29}]^{2+}$, $[Au_{39}(PET)_{29} + 2Cs]^{2+}$, $[Au_{39}(PET)_{29}]^{+}$ and $[Au_{39}(PET)_{29} + Cs]^{+}$, respectively; note that the charges are generated by electrospray or adduction of Cs^+ ions, while the native $Au_{39}(PET)_{29}$ is charge-neutral. The experimental isotope patterns match well with the calculated ones (Fig. 1B). It is worth noting that a decade ago, Meng *et al.* observed the $Au_{39}(PET)_{29}$ NC in ESI-MS analysis of a size-mixed product, but no pure $Au_{39}(PET)_{29}$ was isolated from the mixture[56] because the TLC method for isolating NCs had not been developed until later work.[57] Thus, molecularly pure $Au_{39}(PET)_{29}$ is for the first time achieved in the current work, which permits a detailed study on its PL properties (*vide infra*). Crystallization of $Au_{39}(PET)_{29}$ unfortunately has no success yet, thus, its structure is still unknown.

Optical properties of $Au_{39}(PET)_{29}$

To characterize the optical properties of Au_{39}, we use $CDCl_3$ as the solvent because it has weaker NIR absorption (*i.e.*, vibrational overtones) than other solvents and can thus alleviate the solvent absorption effect; the latter distorts the peaks of NCs. The dissolved $Au_{39}(PET)_{29}$ (abbrev. Au_{39} hereafter) in

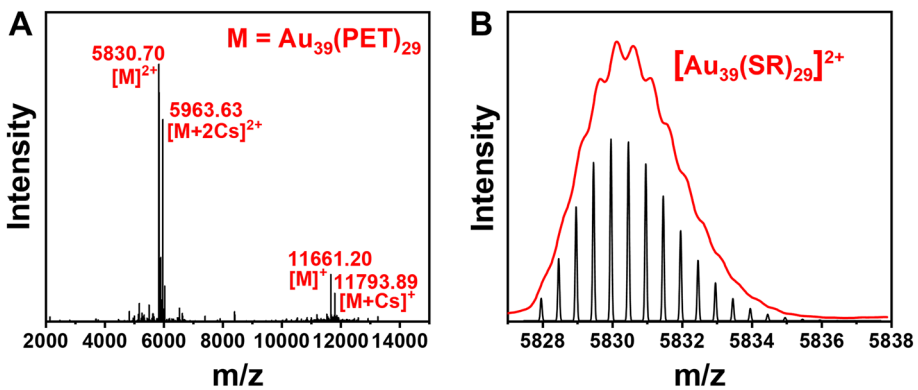

Fig. 1 (A) ESI mass spectrum of $Au_{39}(PET)_{29}$ (CsOAc was added to facilitate ESI analysis); (B) experimental isotope pattern (red profile) of *m/z* at 5830.70 (corresponding to $[Au_{39}(SR)_{29}]^{2+}$ according to the spacing of 0.5, red profile) and the theoretical pattern (black).

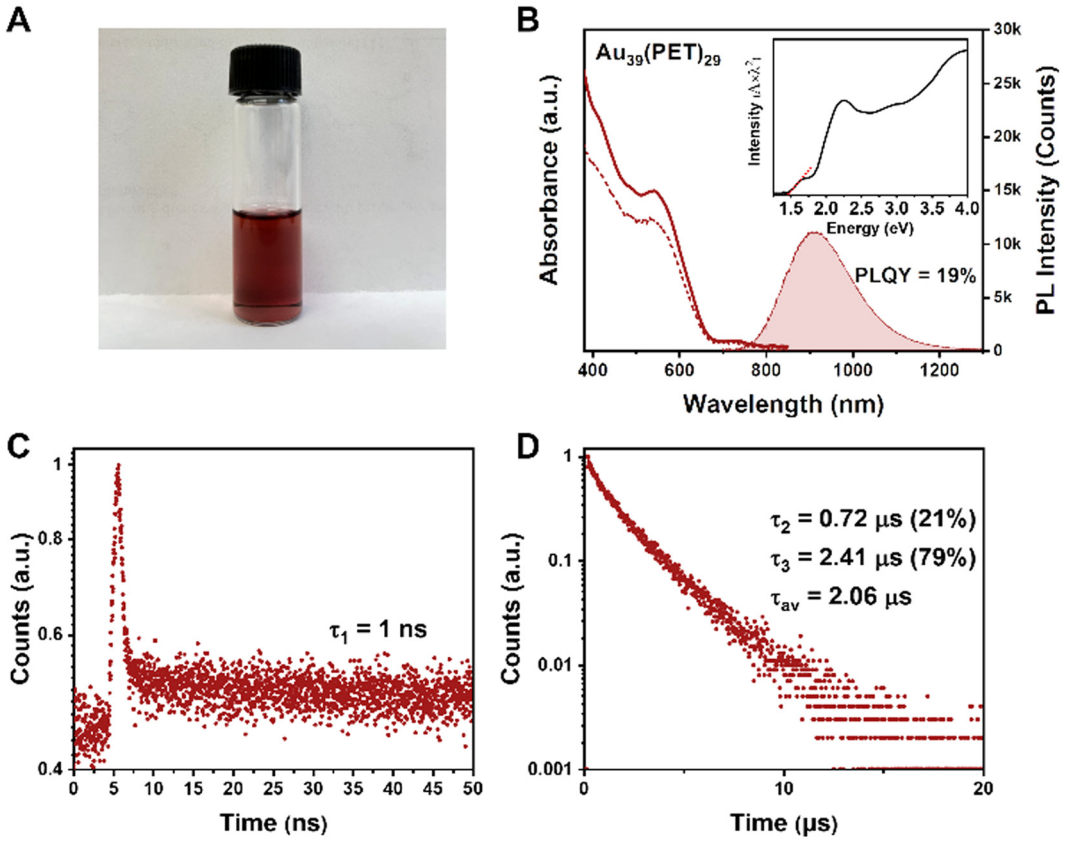

Fig. 2 (A) A photo of $Au_{39}(PET)_{29}$ dissolved in $CDCl_3$. (B) UV-vis absorption (solid line), PL excitation (dashed line) and PL emission (shaded) spectra of Au_{39}. (C) PL decay profile measured on the 50 ns scale (by TCSPC mode). (D) Decay profile measured on the 20 μs scale (by MCS mode). For PL measurements: excitation at 400 nm, slit width 5 nm, and emission slit 5 nm. Deaerated $CDCl_3$ (with N_2 or helium) solutions of Au_{39} NCs were used in all optical measurements unless otherwise noted.

$CDCl_3$ is a dark red solution (Fig. 2A), with the UV-vis absorption spectrum shown in Fig. 2B (solid line). Two main absorption peaks are centered at 534 and 730 nm. The optical gap of Au_{39} is determined to be 1.46 eV by extrapolating the lowest energy absorption peak to zero absorbance (Fig. 2B, inset).

The Au_{39} NC exhibits quite intense PL in the NIR region. Under 400, 534 or 730 nm excitation, Au_{39} shows an identical emission peak at 915 nm (Fig. 2B, the shaded area). The dashed line in Fig. 2B shows the photoluminescence excitation (PLE) spectrum, which is consistent with the absorption profile, indicating that the emission is from the core and its first excited state.[54,58] The PLQY of Au_{39} in deaerated $CDCl_3$ is measured to be 19% by the absolute method using an integrating sphere (Fig. S2†) and 17% under ambient conditions.

Interestingly, although only a single peak is observed in the emission spectrum, time-resolved PL measurements in nanosecond and microsecond regimes show multiple components (Fig. 2C and D). Of note, the microsecond decay was measured by the multi-channel scaling (MCS) single photon counting mode, whereas the nanosecond lifetime was determined by the time-correlated single-photon counting (TCSPC) mode. The resolution of MCS is 10 ns, which is why the PL components shorter than 10 ns cannot be observed in Fig. 2D. The TCSPC mode has a resolution of 0.4 ns (excitation pulses ~100 ps), and the decay curve in the nanosecond regime suggests the existence of a 1 ns (denoted τ_1) lifetime (Fig. 2C). In contrast, the decay curve in the microsecond time regime requires a biexponential function for fitting, *i.e.*, 0.72 μs (τ_2) and 2.41 μs (τ_3). The fitting residuals are of 3σ or smaller (σ = standard deviation). The intensity-averaged lifetime is calculated to be 2.06 μs (Fig. 2D). A comparison of PL spectra for Au_{39} in different solvents is given in Fig. S3,† from which one can see that the solvent effect on the PL spectra is negligible.

Under the O_2 atmosphere, the PL intensity of Au_{39} was found to be slightly suppressed to 87% (Fig. 3A), and the characteristic phosphorescence from singlet oxygen ($^1O_2$, an excited state of $^3O_2$) was observed at 1273 nm (Fig. 3A, inset), suggesting that the PL of Au_{39} involves a contribution from phosphorescence. The lifetime measurements showed that τ_3 is shortened to 1.92 μs while the other two components remain almost the same (Fig. 3B and C). It is widely acknowledged that the lifetime of fluorescence is on the nanosecond scale and the lifetime of phosphorescence is typically over one microsecond.[11,15,40,47] Therefore, by combining the measured lifetimes with the observed oxygen dependence or independence, we assign τ_1 as fluorescence from the first singlet state

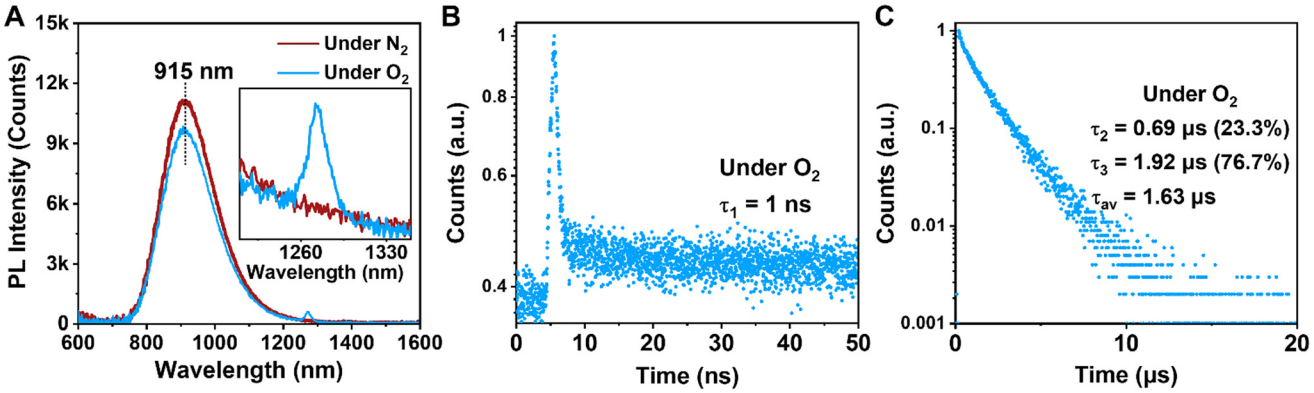

Fig. 3 (A) PL spectra of Au_{39} under N_2 atmosphere (dark red line) and O_2 atmosphere (blue line). Inset shows the expanded region where singlet O_2 emits. (B) Decay profile measured on the 50 ns scale (measured by TCSPC). (C) Decay profile measured on the 20 µs scale (measured by MCS).

(S_1) and τ_3 as phosphorescence from the first triplet state (T_1). The origin of τ_2 is intriguing and to be discussed below. It is worth noting that the quench of phosphorescence under O_2 is commonly not complete for metal NCs as reported by Mitsui *et al.*[59] due to a combination of several factors, including low solubility and slow diffusion rate of oxygen in organic solvents, inefficient charge transfer or energy exchange between metal NCs and oxygen. The existence of a microsecond lifetime component under the O_2 atmosphere supports that the phosphorescence of Au_{39} is not completely quenched by oxygen. The oxygen quenching rate k_q is estimated to be 1.1×10^7 $s^{-1}M^{-1}$ by $\tau = 1/(k_r + k_{nr} + [O_2]k_q)$ using the experimental results of τ at oxygen concentrations $[O_2] = 0$ (for the N_2 case) and 11.5 mM (for the O_2 case).

Temperature-dependent PL analysis

Given the fact that there is no observation of emission from higher excited states, τ_2 should arise from the first excited state. To fully understand the electron dynamics, we carried out temperature-dependent PL measurements from room temperature down to 80 K using liquid nitrogen as the cryogen. The Au_{39} NCs were dissolved in 2-methyl-tetrahydrofuran (abbrev. 2-methyl-THF) for 'glass' formation at cryogenic temperatures. The sample chamber of cryostats was filled with helium gas during the measurements to avoid the interference from oxygen.

With decreasing temperature from 298 K to 80 K, we observed a blue shift of the PL peak and its narrowing (from 310 to 180 meV, full width at half maximum) but no splitting of the emission peak during the entire measurements (Fig. S4A†). The PL intensity of Au_{39} was found to increase by 5 times from 298 K to 80 K, indicating a near unity PLQY at 80 K. Time-resolved PL measurements were performed in the same temperature range to trace the evolution of τ_2 (Fig. 4A and Fig. S5, S6†). The lifetime fitting results are listed in Table 1, and the average lifetime is plotted in Fig. 4A inset. As shown in Table 1, all three lifetime components are found to increase from 298 K to 160 K. Interestingly, when the temperature was 120 K and lower, τ_2 disappeared while τ_1 and τ_3 still remained. The disappearance of τ_2 at low temperatures is attributed to a thermally activated kinetic process.[10,48,60,61] We also embedded Au_{39} NCs in a polystyrene (PS) thin-film and measured the film's temperature-dependent PL spectra (Fig. S4B†). Similar to the solution sample, we observed a gradual blueshift of the peak position, an enhancement of PL intensity, and peak narrowing as the temperature decreases.

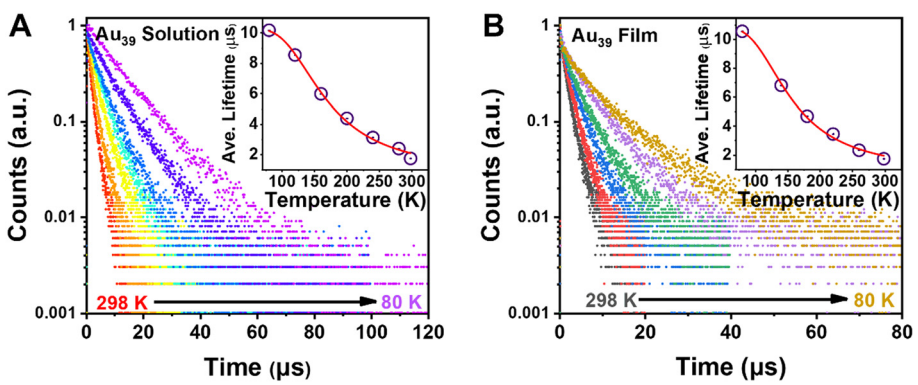

Fig. 4 (A) Temperature-dependent PL decay profiles of Au_{39} in 2-methyl-THF with excitation at 400 nm. Inset: plot of average lifetime and fitting by eqn (2). (B) Temperature-dependent PL decay profiles of Au_{39} in films. Inset: plot of average lifetime and fitting by eqn (2) (see main text).

Table 1 Fitted lifetimes of PL decays of $Au_{39}(PET)_{29}$ in 2-methyl-THF at different temperatures. The percentages in the parentheses indicate the intensity contributions (*i.e.*, photon number%) of each component to the overall intensity. τ_{av} is the averaged lifetime (note: ignoring the weak τ_1 emission)

Temperature	τ_1 (ns) weak	τ_2 (μs)	τ_3 (μs)	τ_{av} (μs)
298 K	0.94	0.87 (37.9%)	2.29 (62.1%)	1.75
280 K	0.93	1.27 (40.7%)	3.19 (59.3%)	2.4
240 K	0.95	1.95 (40.9%)	4.01 (59.1%)	3.13
200 K	1.18	2.61 (28.8%)	5.12 (71.2%)	4.39
160 K	1.31	2.72 (17.3%)	6.68 (82.7%)	5.99
120 K	1.60	None	8.55 (100%)	8.55
80 K	1.68	None	10.18 (100%)	10.18

The PL excitation spectrum for Au_{39} in thin films at 80 K is consistent with its 2-methyl-THF counterpart (Fig. S7†). Furthermore, temperature-dependent PL decays were measured (Fig. 4B and Fig. S8, S9†) and quantitative analysis found that all three lifetime components remained at 80 K (Table 2), suggesting that the kinetic process for τ_2 can be affected by overlapping of excited state wavefunctions in the thin film,[40] resulting in τ_2 survival in the film state, but not in the solution state.

Mechanistic insights

Combining the results of the room temperature steady-state PL spectra and temperature-dependent PL, we assign τ_2 to a TADF process. The mechanism is shown in Scheme 1A–C. Thus, the PL peak of Au_{39} at room temperature consists of three radiative processes (Scheme 1A): nanosecond (τ_1) prompt fluorescence (PF, weak), sub-microsecond (τ_2) TADF, and microsecond (τ_3) phosphorescence (intense). Normally, in organic TADF materials, only PF and TADF can be observed due to weak spin–orbit coupling, but in gold nanoclusters, the heavy gold atoms provide strong spin–orbit coupling, which enables an efficient T_1 to S_0 transition, hence, strong phosphorescence. Among the three components, the low signal-to-noise ratio for τ_1 (Fig. 2C) indicates that the contribution from the PF is much smaller than the other two emission processes. From the relative intensities (see the % values in Table 2), phosphorescence is the main radiative process that contributes to the PL spectra. We calculated the radiative rate at different temperatures. As shown in Fig. S10,† the radiative rate decreases as the temperature decreases, which is typical of TADF materials and thus supports the existence of TADF in Au_{39} NCs.[10,12,62]

Table 2 Fitted lifetimes of PL decays of $Au_{39}(PET)_{29}$/PS film at different temperatures. The percentages in the parentheses indicate the intensity contributions (*i.e.*, photon number%) of each component to the overall intensity. τ_{av} is the intensity averaged lifetime (note: ignoring the weak τ_1 emission)

Temperature	τ_1 (ns) weak	τ_2 (μs)	τ_3 (μs)	τ_{av} (μs)
298 K	1.23	0.55 (16.7%)	1.99 (83.3%)	1.75
260 K	1.50	1.38 (26.2%)	2.68 (73.8%)	2.34
220 K	1.18	1.87 (32.9%)	4.24 (67.1%)	3.46
180 K	1.45	2.10 (24.5%)	5.53 (75.5%)	4.69
140 K	1.4	2.53 (20.4%)	7.91 (79.6%)	6.81
80 K	1.33	4.22 (22.1%)	12.34 (77.9%)	10.55

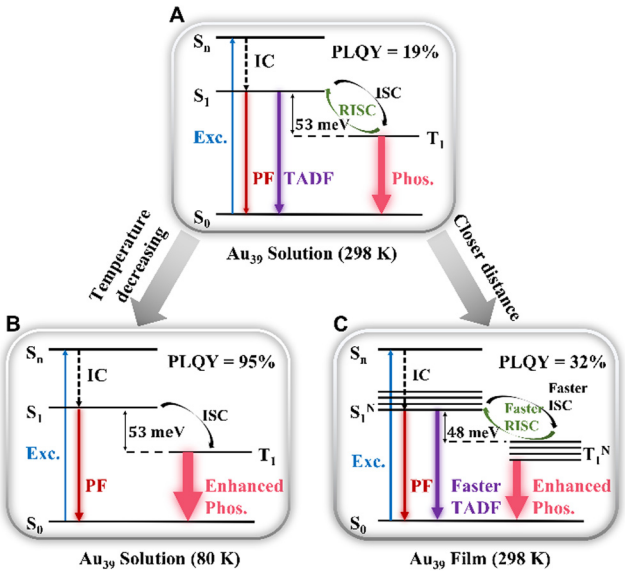

Scheme 1 Emission mechanism of Au_{39} NCs in (A) solution (298 K), (B) solution (80 K), and (C) film (298 K).

The temperature dependent trends of all three radiative components in Au_{39} solution are drawn in Scheme 1B. As the temperature decreases, the PF is only affected by the suppression of non-radiative relaxation between S_1 and S_0 (denoted as k_{nr}^S) which should lead to a monotonic trend. The suppression of k_{nr}^S will have an equal effect on the temperature-dependent TADF. Moreover, the temperature dependence of reverse intersystem crossing (k_{RISC}) follows an Arrhenius formula (eqn (1)):[63,64]

$$k_{RISC}(T) = A\exp\left(-\frac{\Delta E_{S-T}}{k_B T}\right) \quad (1)$$

where, k_{RISC}(T) indicates the temperature dependent k_{RISC}, A is a pre-exponential constant, ΔE_{S-T} is the energy gap between S_1 and T_1, and k_B is the Boltzmann constant. The Arrhenius formula suggests that k_{RISC} will be suppressed and lead to a dramatic decrease of TADF when the temperature is sufficiently low. Therefore, the temperature-dependent trend of TADF is expected to experience a counteraction between the k_{nr}^S and k_{RISC} factors, and below 140 K the suppression of k_{RISC} overwhelms the suppression of k_{nr}^S, hence, the vanishing of TADF. As for the phosphorescence, the suppression of k_{RISC} will increase the population of T_1 state and hence an increase of the phosphorescence percentage at low temperatures. Meanwhile, the suppression of non-radiative relaxation between T_1 and S_0 (denoted k_{nr}^T) also results in an increase of phosphorescence intensity when the temperature decreases, resulting in nearly 100% phosphorescece at cryogenic temperatures (Scheme 1B); note: the PF is weak in Au_{39} and negligible.

The observed temperature-dependent trend of Au_{39} NCs in 2-methyl-THF is different from the typical trend of organic

TADF; for the latter, a decrease in TADF and a peak redshift would be observed. Here we further explain the Au_{39} results as follows. First, unlike organic TADF that exhibits no phosphorescence, phosphorescence is the main radiative process in Au_{39} NCs and it shows a monotonic increase as the temperature drops. The increase of phosphorescence is able to completely offset the decrease of TADF; thus, resulting in a continuous net increase of the total PL intensity (Fig. S4A†). The emission peak has a mix of three components above 140 K, but mainly the phosphorescence below 140 K. In Au_{39}, the energy gap between S_1 and T_1 is extremely small (*i.e.*, of meV, see below) as opposed to ~0.2 eV in organic TADF, and the meV gap is overwhelmed by an enlargement (spectroscopically a blueshift) of the energy gap from the suppression of electron–phonon interaction[37] when the temperature decreases, hence, a net blueshift of the peak position observed with decreasing temperature.

The kinetic process of Au_{39} NCs in the PS thin-film is shown in Scheme 1C. Similar to the solution phase, Au_{39} in PS thin-films also consists of three radiative processes but with a different ratio. As shown in Fig. S11,† the PLQY of Au_{39} NCs in PS thin-film is increased by 1.7 times, that is, 32%. The increase of PLQY in the Au_{39}/PS thin-film can be ascribed to the suppression of surface staple vibrations in the solid-state.[37,65] The existence of τ_2 (*i.e.*, TADF) in the Au_{39}/PS thin-film even down to 80 K suggests that the reverse intersystem crossing is not yet sufficiently suppressed at this temperature (*cf.* the disappearance of τ_2 at 120K in the solution system). We ascribe it to the strong dipole–dipole interaction in the solid-state because all NCs possess a dipole moment[66] and they are much closer in the film than in solution. Such an interaction will lead to a narrowing of the energy gap between S_1 and T_1.[40,67] Following the Arrhenius formula, a smaller ΔE_{S-T} will benefit both k_{ISC} and k_{RISC}, hence, stronger TADF and phosphorescence. To completely suppress the RISC (k_{RISC}) in the film state, a lower temperature than 80 K is needed, as opposed to the 140 K at which TADF is quenched in the solution system.

Here we estimate the singlet–triplet gap in Au_{39}. Under the assumption of degenerate triplet states, an estimation of the ΔE_{S-T} can be given by fitting the intensity average lifetime to eqn (2):[61]

$$\tau_{av} = \frac{3 + \exp\left[-\frac{\Delta E_{S-T}}{k_B T}\right]}{\frac{3}{\tau(T_1)} + \frac{1}{\tau(S_1)}\exp\left[-\frac{\Delta E_{S-T}}{k_B T}\right]} \quad (2)$$

where, ΔE_{S-T} is the energy gap between S_1 and T_1, $\tau(S_1)$ and $\tau(T_1)$ is the intrinsic lifetime of S_1 and T_1 states, and k_B is the Boltzmann constant. The fitting line is plotted in the inset of Fig. 4A and B, and the extracted parameters are given in Table 3. This estimation shows that ΔE_{S-T} in the Au_{39}/PS thin-film is ~10% smaller than that in the Au_{39} solution, supporting our inference above. It is worth commenting on the distinct differences between nanoclusters and organic TADF materials. First, the energy gap between S_1 and T_1 in NCs is extremely small (*e.g.*, ~50 meV). Second, the heavy atoms (*e.g.* Au_{39}) result in strong spin–orbit coupling. Both factors significantly increase the ISC/RISC rates and make phosphorescence coexist with TADF in the NCs at room temperature.

Table 3 Fitted parameters for $Au_{39}(PET)_{29}$ solution and $Au_{39}(PET)_{29}$ film according to eqn (2) and the temperature dependent PL data in Fig. 4

Temperature	ΔE_{S-T}	$\tau(S_1)$/ns	$\tau(T_1)$/μs
$Au_{39}(PET)_{29}$ solution	53	107	10.3
$Au_{39}(PET)_{29}$/PS film	48	113	10.8

Conclusion

In summary, we have synthesized a molecularly pure $Au_{39}(PET)_{29}$ nanocluster exhibiting strong near-infrared (915 nm) luminescence with QY of 19% in solution and 32% in films at room temperature, which is the highest in the NIR region among the thiolate-protected gold NCs. The steady-state and time-resolved PL measurements, as well as temperature-dependent PL measurements reveal that the single-peak emission of $Au_{39}(PET)_{29}$ consists of prompt fluorescence (weak), thermally activated delayed fluorescence, and phosphorescence (strong), and their merge into a single emission peak is due to the extremely small singlet–triplet gap (~50 meV). Phosphorescence is identified to be the main contributor to the observed strong photoluminescence. Compared to the solution phase, $Au_{39}(PET)_{29}$ NCs in the solid-state have the suppressed surface vibrations and stronger dipolar interactions; the latter lead to a narrowing of the gap between S_1 and T_1 states. Both effects lead to a higher QY (32%, at room temperature) with predominant phosphorescence. The QYs of both the solution and film of Au_{39} reach near unity at 80 K. Overall, such NCs hold promise as a new class of luminescent (TADF/phosphorescent) materials having ultrafast ISC/RISC and short emission lifetimes (~1 μs), which can potentially overcome the issue of roll-off of emitting efficiency in organic TADF devices and also extend to the NIR wavelengths for special applications.

Conflicts of interest

The authors declare no competing financial interest.

Acknowledgements

R. J. acknowledges the financial support from the Kaufman Foundation.

References

1 R. Jin, C. Zeng, M. Zhou and Y. Chen, *Chem. Rev.*, 2016, **116**, 10346–10413.

2 I. Chakraborty and T. Pradeep, *Chem. Rev.*, 2017, **117**, 8208–8271.
3 K. Pyo, V. D. Thanthirige, K. Kwak, P. Pandurangan, G. Ramakrishna and D. Lee, *J. Am. Chem. Soc.*, 2015, **137**, 8244–8250.
4 Y. Zhong, J. Zhang, T. Li, W. Xu, Q. Yao, M. Lu, X. Bai, Z. Wu, J. Xie and Y. Zhang, *Nat. Commun.*, 2023, **14**, 658.
5 G. Deng, K. Lee, H. Deng, S. Malola, M. S. Bootharaju, H. Häkkinen, N. Zheng and T. Hyeon, Alkynyl-Protected Chiral Bimetallic $Ag_{22}Cu_7$ Superatom with Multiple Chirality Origins, *Angew. Chem., Int. Ed.*, 2023, **62**, e202217483.
6 X. Kang and M. Zhu, *Chem. Soc. Rev.*, 2019, **48**, 2422–2457.
7 J. Dong, Z. Gan, W. Gu, Q. You, Y. Zhao, J. Zha, J. Li, H. Deng, N. Yan and Z. Wu, *Angew. Chem., Int. Ed.*, 2021, **60**, 17932–17936.
8 Y. Li, M. Zhou, Y. Song, T. Higaki, H. Wang and R. Jin, *Nature*, 2021, **594**, 380–384.
9 J. J. Li, C. Y. Liu, Z. J. Guan, Z. Lei and Q. M. Wang, *Angew. Chem.*, 2022, **134**, e202201549.
10 X. S. Han, X. Luan, H. F. Su, J. J. Li, S. F. Yuan, Z. Lei, Y. Pei and Q. M. Wang, *Angew. Chem.*, 2020, **132**, 2329–2332.
11 M. Mitsui, D. Arima, Y. Kobayashi, E. Lee and Y. Niihori, *Adv. Opt. Mater.*, 2022, **10**, 2200864.
12 Z.-R. Yuan, Z. Wang, B.-L. Han, C.-K. Zhang, S.-S. Zhang, Z.-Y. Zhu, J.-H. Yu, T.-D. Li, Y.-Z. Li, C.-H. Tung and D. Sun, *Angew. Chem., Int. Ed.*, 2022, **61**, e202211628.
13 J. W. Fagan, K. D. M. Weerawardene, A. Cirri, C. M. Aikens and C. J. Johnson, *J. Chem. Phys.*, 2021, **155**, 014301.
14 D. Bain, S. Maity, T. Debnath, A. K. Das and A. Patra, *Mater. Res. Express*, 2019, **6**, 124004.
15 M. Sugiuchi, J. Maeba, N. Okubo, M. Iwamura, K. Nozaki and K. Konishi, *J. Am. Chem. Soc.*, 2017, **139**, 17731–17734.
16 E. Khatun, M. Bodiuzzaman, K. S. Sugi, P. Chakraborty, G. Paramasivam, W. A. Dar, T. Ahuja, S. Antharjanam and T. Pradeep, *ACS Nano*, 2019, **13**, 5753–5759.
17 M. S. Bootharaju, C. P. Joshi, M. R. Parida, O. F. Mohammed and O. M. Bakr, *Angew. Chem.*, 2016, **128**, 934–938.
18 M.-M. Zhang, X.-Y. Dong, Z.-Y. Wang, X.-M. Luo, J.-H. Huang, S.-Q. Zang and T. C. Mak, *J. Am. Chem. Soc.*, 2021, **143**, 6048–6053.
19 S.-S. Zhang, S. Havenridge, C. Zhang, Z. Wang, L. Feng, Z.-Y. Gao, C. M. Aikens, C.-H. Tung and D. Sun, *J. Am. Chem. Soc.*, 2022, **144**, 18305–18314.
20 P. J. Herbert, C. J. Ackerson and K. L. Knappenberger Jr., *J. Phys. Chem. Lett.*, 2021, **12**, 7531–7536.
21 C. Zhu, J. Xin, J. Li, H. Li, X. Kang, Y. Pei and M. Zhu, *Angew. Chem., Int. Ed.*, 2022, **61**, e202205947.
22 A. T. Rad, Y. Bao, H. S. Jang, Y. Xia, H. Sharma, E. E. Dormidontova, J. Zhao, J. Arora, V. T. John, B. Z. Tang, T. Dainese, A. Hariri, J. V. Jokerst, F. Maran and M.-P. Nieh, *Adv. Funct. Mater.*, 2021, **31**, 2009750.
23 Y. Huang, K. Chen, L. Liu, H. Ma, X. Zhang, K. Tan, Y. Li, Y. Liu, C. Liu, H. Wang and X.-D. Zhang, *Small*, 2023, 2300145.
24 H. Liu, G. Hong, Z. Luo, J. Chen, J. Chang, M. Gong, H. He, J. Yang, X. Yuan and L. Li, *Adv. Mater.*, 2019, **31**, 1901015.
25 T.-Q. Yang, B. Peng, B.-Q. Shan, Y.-X. Zong, J.-G. Jiang, P. Wu and K. Zhang, *Nanomaterials*, 2020, **10**, 261.
26 Q. Li, C. J. Zeman IV, G. C. Schatz and X. W. Gu, *ACS Nano*, 2021, **15**, 16095–16105.
27 L. Liao, C. Wang, S. Zhuang, N. Yan, Y. Zhao, Y. Yang, J. Li, H. Deng and Z. Wu, *Angew. Chem., Int. Ed.*, 2020, **59**, 731–734.
28 K. Konishi, M. Iwasaki and Y. Shichibu, *Acc. Chem. Res.*, 2018, **51**, 3125–3133.
29 M. Zhou and Y. Song, *J. Phys. Chem. Lett.*, 2021, **12**, 1514–1519.
30 Q. Li, M. Zhou, W. Y. So, J. Huang, M. Li, D. R. Kauffman, M. Cotlet, T. Higaki, L. A. Peteanu, Z. A. Shao, *et al.*, *J. Am. Chem. Soc.*, 2019, **141**, 5314–5325.
31 X. Jiang, B. Du, Y. Huang and J. Zheng, *Nano Today*, 2018, **21**, 106–125.
32 B. Du, X. Jiang, A. Das, Q. Zhou, M. Yu, R. Jin and J. Zheng, *Nat. Nanotechnol.*, 2017, **12**, 1096–1102.
33 C. Zeng, Y. Chen, A. Das and R. Jin, *J. Phys. Chem. Lett.*, 2015, **6**, 2976–2986.
34 S. Gratious, S. Mukherjee and S. Mandal, *J. Phys. Chem. Lett.*, 2022, **13**, 9014–9027.
35 S. Mukherjee, D. Jayakumar and S. Mandal, *J. Phys. Chem. C*, 2021, **125**, 12149–12154.
36 T. D. Green, C. Yi, C. Zeng, R. Jin, S. McGill and K. L. Knappenberger Jr., *J. Phys. Chem. A*, 2014, **118**, 10611–10621.
37 Z. Liu, Y. Li, E. Kahng, S. Xue, X. Du, S. Li and R. Jin, *ACS Nano*, 2022, **16**, 18448–18458.
38 M. Zhou, C. Zeng, M. Y. Sfeir, M. Cotlet, K. Iida, K. Nobusada and R. Jin, *J. Phys. Chem. Lett.*, 2017, **8**, 4023–4030.
39 M. Suyama, S. Takano and T. Tsukuda, *J. Phys. Chem. C*, 2020, **124**, 23923–23929.
40 L. Luo, Z. Liu, X. Du and R. Jin, *J. Am. Chem. Soc.*, 2022, **144**, 19243–19247.
41 Z. Wu, Q. Yao, S.-Q. Zang and J. Xie, *Natl. Sci. Rev.*, 2021, **8**, nwaa208.
42 N. Goswami, Q. Yao, Z. Luo, J. Li, T. Chen and J. Xie, *J. Phys. Chem. Lett.*, 2016, **7**, 962–975.
43 Z. Han, X. Zhao, P. Peng, S. Li, C. Zhang, M. Cao, K. Li, Z.-Y. Wang and S.-Q. Zang, *Nano Res.*, 2020, **13**, 3248–3252.
44 Z. Wu, Q. Yao, O. J. H. Chai, N. Ding, W. Xu, S. Zang and J. Xie, *Angew. Chem.*, 2020, **132**, 10020–10025.
45 S. Jin, W. Liu, D. Hu, X. Zou, X. Kang, W. Du, S. Chen, S. Wei, S. Wang and M. Zhu, *Chem. – Eur. J.*, 2018, **24**, 3712–3715.
46 W.-D. Si, K. Sheng, C. Zhang, Z. Wang, S.-S. Zhang, J.-M. Dou, L. Feng, Z.-Y. Gao, C.-H. Tung and D. Sun, *Chem. Sci.*, 2022, **13**, 10523–10531.
47 S. Takano, H. Hirai, T. Nakashima, T. Iwasa, T. Taketsugu and T. Tsukuda, *J. Am. Chem. Soc.*, 2021, **143**, 10560–10564.
48 H. Hirai, S. Takano, T. Nakashima, T. Iwasa, T. Taketsugu and T. Tsukuda, *Angew. Chem., Int. Ed.*, 2022, **61**, e202207290.

49 Z. Wu and R. Jin, *Nano Lett.*, 2010, **10**, 2568–2573.
50 K. Sahoo and I. Chakraborty, *Nanoscale*, 2023, **15**, 3120–3129.
51 C. Yao, S. Tian, L. Liao, X. Liu, N. Xia, N. Yan, Z. Gan and Z. Wu, *Nanoscale*, 2015, **7**, 16200–16203.
52 B. Zhang, J. Chen, Y. Cao, O. J. H. Chai and J. Xie, *Small*, 2021, **17**, 2004381.
53 M. R. Narouz, S. Takano, P. A. Lummis, T. I. Levchenko, A. Nazemi, S. Kaappa, S. Malola, G. Yousefalizadeh, L. A. Calhoun and K. G. Stamplecoskie, *J. Am. Chem. Soc.*, 2019, **141**, 14997–15002.
54 M. Zhou, T. Higaki, G. Hu, M. Y. Sfeir, Y. Chen, D.-E. Jiang and R. Jin, *Science*, 2019, **364**, 279–282.
55 Q. Li, D. Zhou, J. Chai, W. Y. So, T. Cai, M. Li, L. A. Peteanu, O. Chen, M. Cotlet, X. W. Gu, *et al.*, *Nat. Commun.*, 2020, **11**, 2897.
56 X. Meng, Z. Liu, M. Zhu and R. Jin, *Nanoscale Res. Lett.*, 2012, **7**, 277.
57 S. Tian, Y.-Z. Li, M.-B. Li, J. Yuan, J. Yang, Z. Wu and R. Jin, *Nat. Commun.*, 2015, **6**, 8667.
58 K. D. M. Weerawardene and C. M. Aikens, *J. Am. Chem. Soc.*, 2016, **138**, 11202–11210.
59 M. Mitsui, D. Arima, A. Uchida, K. Yoshida, Y. Arai, K. Kawasaki and Y. Niihori, *J. Phys. Chem. Lett.*, 2022, **13**, 9272–9278.
60 A. D. Wright, C. Verdi, R. L. Milot, G. E. Eperon, M. A. Pérez-Osorio, H. J. Snaith, F. Giustino, M. B. Johnston and L. M. Herz, *Nat. Commun.*, 2016, **7**, 11755.
61 T. Hofbeck, U. Monkowius and H. Yersin, *J. Am. Chem. Soc.*, 2015, **137**, 399–404.
62 Y. Wang, Z. Liu, A. Mazumder, C. G. Gianopoulos, K. Kirschbaum, L. A. Peteanu and R. Jin, *J. Am. Chem. Soc.*, 2023, **145**, 26328–26338.
63 A. Niwa, T. Kobayashi, T. Nagase, K. Goushi, C. Adachi and H. Naito, *Appl. Phys. Lett.*, 2014, **104**, 213303.
64 N. Aizawa, Y.-J. Pu, Y. Harabuchi, A. Nihonyanagi, R. Ibuka, H. Inuzuka, B. Dhara, Y. Koyama, K.-I. Nakayama and S. Maeda, *Nature*, 2022, **609**, 502–506.
65 Z. Liu, Y. Li, W. Shin and R. Jin, *J. Phys. Chem. Lett.*, 2021, **12**, 1690–1695.
66 M. J. Cowan, T. Higaki, R. Jin and G. Mpourmpakis, *J. Phys. Chem. C*, 2019, **123**, 20006–20012.
67 M. Kasha, H. R. Rawls and M. A. El-Bayoumi, *Pure Appl. Chem.*, 1965, **11**, 371–392.